IAC–24,C2,3,1,x81243

3D-Printing Mechatronics Components for Reconfigurable Robotics

Kevin Sankar[a*], **Xavier Walls Perez**[b], **Alex Ellery**[c]

[a] *Graduate Student - Department of Mechanical and Aerospace Engineering, Carleton University, Ottawa, Canada, kevinsankar@cmail.carleton.ca*
[b] *Department of Mechanical and Aerospace Engineering, Carleton University, Ottawa, Canada, xavierwallsperez@cmail.carleton.ca*
[c] *Department of Mechanical and Aerospace Engineering, Carleton University, Ottawa, Canada, aellery@mae.carleton.ca*
[*] *Corresponding author*

Abstract

Modularized reconfigurable robotics, using 3D-printed mechatronics components, allows for in-space manufacturing with the potential to transform spacecraft design. This paper focuses on 3D-printing a complete mechatronic system including DC motor, coupling mechanism, and electronic control circuitry to act as an individual module or unit for reconfigurable robotics. These units can be reconfigured to allow for more complex robotic systems with varying degrees of freedom. This is advantageous in space environments where the individual units can be reused to provide a different functionality which reduces payload requirements. This can be expanded upon further by using lunar materials to 3D-print these units in space. The paper models the various mechatronics components and initially prints them using standard and modified plastic filaments. Several topologies were evaluated for the DC motor system to determine the most efficient structure. The electrical control circuity mainly comprises of a H-bridge and PWM generator circuits. A simple potentiometer was used to control the duty cycle of the PWM as a form of open loop control for the DC motor. The 3D-printed individual unit was tested and proven to be a viable prototype, so multiple units can be connected to create more complex robotic systems. This paper discusses some of the components that is required to create an individual unit. The work described in this paper can also be expanded upon for self-replicating machines in a robotic factory.

Acronyms/Abbreviations

ACOR	= Active Connector for Robotic Systems
MRR	= Modular Reconfigurable Robot
PWM	= Pulse-Width Modulation
SMA	= Shape Memory Alloy

1. Introduction

Modular Reconfigurable Robotics (MRR) refers to robotic systems that are composed of several units that are capable of rearranging themselves into different configurations based on the task that needs to be accomplished [1]. MRRs allow for versatility in task completion as a wider array of objectives can be fulfilled using a singular MRR that is composed of a variety of modular reconfigurable units. This is because of their redundant degrees of freedom [1]. The units that compose MRRs are usually in the form of some primary structural actuated module and can include additional units such as cameras, payloads, energy storage and generation modules [2].

Space environments have a many different tasks that are required and often need a variety of robots to accomplish each task [3]. MRRs can allow for modules to be created that can then adjust to different tasks and reduce the costs and payload requirements. If these mechatronic components can be 3D printed using materials that are already found in space, such as materials extracted from lunar regolith, it then means that MRR units can be manufactured in space without the need for launches from Earth.

This paper first investigates the theoretical design choices that were made when designing an MRR unit, followed by an in-depth look at the 3D printing process that was used. The theory and calculations required for the designs were also discussed followed by the results obtained from the physical design and testing process.

2. Theoretical design choices

When designing the MRR units,the first step taken was to select the type of motor that would be used within the module, followed by selecting the sensors that would be included in a sensor suite for the system. The coupling mechanism for the module was also chosen, along with the control circuitry. This section discusses the decisions made with regards to the theoretical design choices.

2.1 Motor selection

Electric motors can be categorized as either (Direct Current) DC motors or (Alternating Current) AC motors depending on how they are powered [4]. Electric motors are composed of two main parts, the stator which is a stationary component and a rotor which is a moving com-

ponent [4]. In AC motors, the stator is supplied with AC current which produces a magnetic field that revolves with accordance to the AC current frequency. Through induction, a magnetic field is formed in the rotor and the interactions of the fields produce rotation and torque [5]. In a typical brushed DC motor, the spinning armature is supplied with DC current through a commutator which makes use of a carbon brush to conduct electricity. The magnetic field of the stator can be supplied by permanent magnets or electromagnets and as the rotor spins, the commutator switches polarity of the electromagnetic field which causes the armature to attract and repel to different parts of the stator [6]. This results in continuous rotations. DC motors can also be brushless which means that rotor is made of a permanent magnet and the stator contains electromagnets that switch polarity and cause the rotor to rotate [7].

The differences that were considered when choosing between AC and DC motors was speed control, efficiency and complexity. AC motors require a Variable Frequency Drive (VFD) in order to change the speed of the motor, which adds complexities and inefficiencies to the system [8], while DC motors are easily speed controlled by adjusting the supply voltage. Since AC motors use electromagnets in the stator, they are generally less efficient than DC motors which often use permanent magnets. Given this knowledge, a DC motor was chosen as it would be less complex to model and allow for fine speed control.

There are two types of DC motors that were considered for this application: brushed and brushless as seen in Fig.1. Brushed DC motors have a quick response and excellent controllability but they also require regular maintenance due the the mechanical contact between the brushes and commutator [9]. Brushless DC motors are long lasting and require no maintenacne, but they are much more complex to design and construct [9]. since, the goal is to 3D print the motor, a simpler structure is preferred and so the brushed DC motor was chosen.

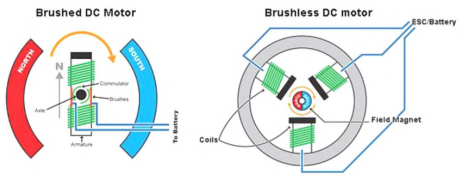

Fig. 1. Brushed and brushless DC motors [10]

The next consideration made with regards to the motor choice, was the topology to be used. The options considered included radial flux and axial flux which are represented in Fig. 2. In radial flux motors the magnetic flux flows perpendicularly to the motor shaft in a radial motion [11]. These motors have a traditional elongated shape with the rotor positioned either inside or outside and consist of traditional laminations and copper windings. In axial flux motors, the magnetic flux flows parallel to the motor shaft [11]. The result of this is a flat design and so the rotor and stator are organized in a disc configuration.

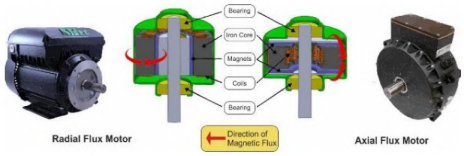

Fig. 2. Radial flux motor and Axial flux motor [12]

A key difference between radial and axial flux motors is the manufacturability. The axial flux motor is a more complex structure to manufacture which may prove to be difficult to achieve using additive manufacturing techniques. Radial flux motors have a very straightforward construction which makes them a more viable option for this application. Radial flux motors also require a reduced volume of permanent magnets when compared to axial flux motors [13]. Hence, the radial flux topology was chosen.

Another consideration that was made was the configuration of the windings as they correspond to the poles. The pole count of a motor refers to the number of permanent magnet pairs that are present within a motor. This means that a 2-pole motor will have one pair of magnets in an opposing north to south configuration while a 4-pole motor has two pairs of magnets that oppose each other [14]. The number of poles that a motor has affects the configuration of the windings and directly affects the output power, rated speed and maximum speed. 2-pole motors have fast magnetic field changes resulting in higher speed and power density. 4-pole motors have a medium speed and power density and relatively slow magnetic field changes. As the number of poles increase, the speed of the motor decreases and the torque increases [14]. Therefore for the application in MRRs, a 4-pole motor is ideal as the speed is not too high and not too strong allowing for an appropriate mid-line. Therefore a 4-pole winding configuration was chosen. Therefore, the final motor design that was chosen for the 3D printed MRR module was a 4-pole DC Brushed Radial Motor.

2.2 Sensor suite

The sensor suite is essentially all of the sensor and electronic components that are used for motor control. The first sensor that was considered for the MRR system

was a rotary potentiometer. Rotary potentiometers are adjustable angle sensors that convert rotary distances into a change in resistance [15]. The rotary potentiometer works by having the internal resistance set as function of the angle that is turned by the knob. The starting position of the knob is pre-set to zero and so the internal resistance can be used to determine the angle turned by the knob [16].

Another sensor that was considered for the sensor suite was the hall effect sensor. This is a sensing technology that is used to transduce magnetic fields to electrical signals. These sensors allow for real-time system monitoring and control, magnetic field strength to position conversion, high-speed rotary encoding and flexible mechanical placement. These are all useful features for MRR modules. Optical encoders are a common type of sensor that are used with motors. They use unique coded patterns to find real-time absolute positions [17]. They are highly accurate sensors and have a wide measurement range that would be incredibly relevant for MMR modules.

Given that the goal of this research is to 3D print MMR modules, a possible option would be to 3D print the sensors that are incorporated into the sensor suite. The work done in [17] shows an example of an optical encoder where the cylindrical coded disk, shaft and support structures were 3D printed and paired with a photo sensor. Hall effect sensors have also been 3D printed as mentioned in [18].

2.3 Coupling mechanisms

The mechanical components of an MRR system require a coupling mechanism for the integration between the separate modules. Reconfiguration of the structures relies on the ease of coupling and decoupling. Autonomous coupling requires advanced sensing and control schemes [19]. The coupling of MRR modules is divided into intra-robot coupling and inter-robot coupling. Intra-robot coupling occurs between modules that are in a connected group. Inter-robot coupling occurs between separate unconnected groups [19]. Different coupling mechanisms can vary in gender, actuation methods, symmetry and misalignment tolerance. The gender of a coupling mechanism refers to connectors that have one interface that actively couples with an opposing passive interface [19]. There can be gendered, bi-gendered or genderless coupling. The actuation methods can vary between motors, electro/permanent magnets or Shape Memory Alloy (SMA) wire. SMAs refer to a class of materials that are capable of recovering their shape after they are deformed at a lower temperature. SMAs are used as an alternative to traditional actuators as they allow for a reduction in weight and size while still producing complex motions [20]. The symmetry of a coupling mechanism depends on the placement of the interface features about the roll axis of the connector [19]. Misalignment tolerance refers to the allowable range of tolerance for modules alignment with opposing interface.

Two coupling mechanisms that were considered for the MRR modules were the active connector for robotic systems (ACOR) and the Roombots mechanism. The ACOR has a male plug and female receptacle,allowing for mechanical and electrical interfacing [21]. Both the plug and receptacle contain flexible lamellae that allow for connections to be made. An SMA actuator is used to move the lamellae so that it can either engage or disengage the coupling mechanism [22]. The model in Fig. 3, shows the cross section for the mechanism and the interlocking lamellae.

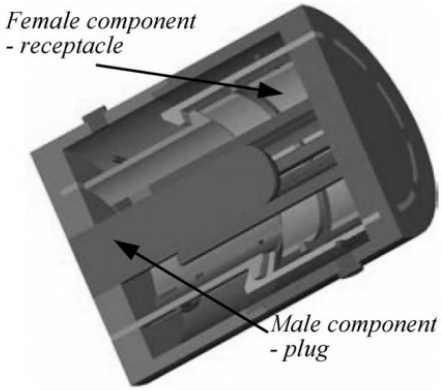

Fig. 3. Cross-Section of the ACOR coupling mechanism [22]

The Roombots coupling mechanism falls under the Hooks family of mechanisms. Each module contains a bi-gendered coupling mechanism that has four hooks and four latching ports. A gear motor is incorporated to allow for latching to occur between the units. Both sides of the connection must be powered in order to undock [19]. Fig. 4 shows the layout for the active coupling mechanism used by Roombots.

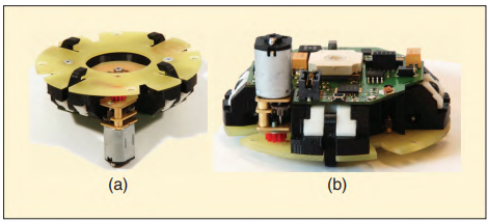

Fig. 4. Roombots active coupling mechanism [23]

The ACOR coupling mechanism was chosen for the 3D printed MRR as it was a simpler mechanism to model and print. However, the Roombots mechanism would still be a viable option for the use-case, it would just need to be adjusted to make it more practical for 3D printing.

2.4 Electronic control circuitry

The final aspect of the MRR modules that was considered was the control circuitry. A common circuit that is used for DC motor control is the H-bridge. This circuit is composed of 4 switches, which can be p-type and n-type MOSFETs as seen in Fig.5, that are connected in an 'H' configuration around the DC motor. They allow for the direction and speed of the motor to be controlled by choosing which of the switches are on and which are off. When the S1 and S4 MOSFETs are turned on, the right lead of the motor becomes grounded and the left lead is powered, allowing the motor to operate in the forward direction. When S2 and S3 are turned on, the opposite occurs [24].

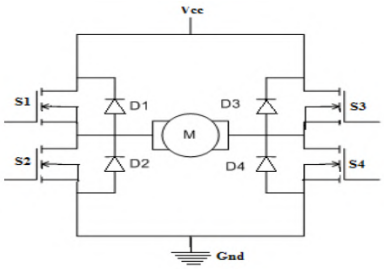

Fig. 5. Simplified H-bridge circuit using MOSFETs [24]

Pulse Width Modulation (PWM) is often used to drive MOSFET gates. PWM allows the speed of the motor to be controlled by controlling the duty cycle. A PWM circuit that can also generate a triangular wave can be formed using the circuit seen in Fig. 6.

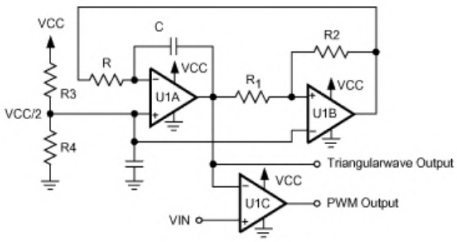

Fig. 6. Circuit capable of generating a Triangular wave and a variable Pulsewidth [25]

In this circuit, U1A and U1B form the triangle wave generator while U1C acts as the comparator with hysteresis [25]. The expected output from this PWM circuit can be seen in Fig.7.

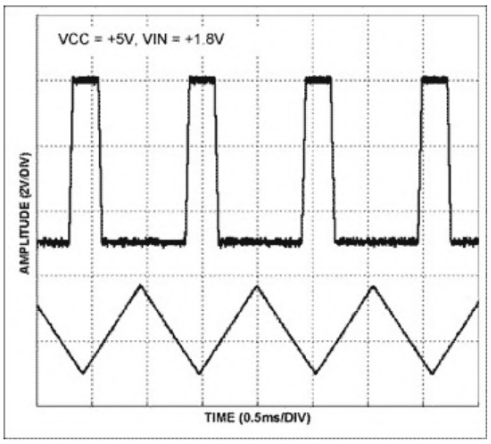

Fig. 7. PWM and Triangular Waveform resulting from the PWM Circuit [25]

This circuit was chosen along with the H-bridge as the control circuitry for the MRR 3D printed module. Given the nature of the application of the MRRs, it is important to investigate the implementation of all aspects of the system at the lowest level. An analog P-controller was investigated to work along with the other chosen control circuitry. The work done in [26] shows how a Proportional, Integral and Derivative (PID) controller was designed using analog components such as operational amplifiers. This concept was investigated for Proportional or P controllers in this paper. P controllers work to minimize errors proportionally to the difference between a desired value and a measured value.

Another aspect of the system that requires a control strategy, outside of the motor, is the SMA actuator used in the ACOR coupling mechanism. Electrical resistance feedback is a successful control strategy that is simple to apply and allows for a reference resistor value to be used as an indicator of full actuation. this method prevents overextension and overheating of the SMA wire [27]. Given the simplicity and ease of implementation, this control method was chosen for the SMA wire actuator.

All of the control mechanisms used in this paper are manual through the use of pushbuttons or potentiometers. This is done so as to ensure the lowest level of implementation with basic analog components and no digital components.

3. 3D-printing process

3.1 Design and modelling

An off-the-shelf commercial DC motor was purchased to act as a basis for the motor design and modelling. This motor was disassembled to reveal the internal structure including the permanent magnets, rotor, coils and commutator (see Fig. 8).

Fig. 8. Internal structure of DC motor

From the disassembly, it was observed that the motor was a 2-pole using arc shaped magnets along with 3 coils and associated segments on the commutator ring. The main benefits of the three coils is that it allows for smoother operation and provides a more compact size. Based on this disassembly and from theory, the designed 3d-printed motor will have 4-poles (two north and two south), 4 coils, and 4 associated segments on the commutator. This configuration will sacrifice weight and size to provide higher output power and better torque characteristics.

Based on the findings from the disassembled DC motor, the rotor and stator of the 3d-printed motor were designed and modelled using Autodesk Fusion. The rotor was sized to appropriately to fit an arbitrarily chosen value of 50 turns for each coil. A 3mm diameter through-hole was used in the rotor and commutator for the motor shaft. The stator was constrained by the height of the 3d-printed magnets and featured rectangular mounting holes on the top and bottom to allow the remaining components of the modular unit to be friction fitted. All dimensions with respect to the rotor, stator, and commutator are shown in Table 1, and the 3d-models can be seen in Fig.9.

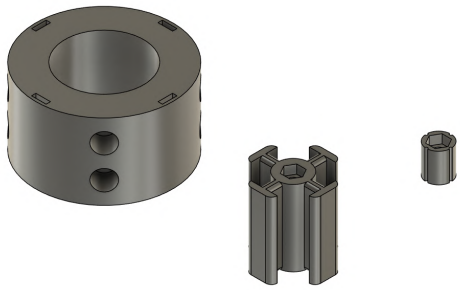

Fig. 9. 3D Models of Rotor, Stator, Commutator

Table 1. Dimensions of Rotor, Stator, and Commutator

	Dimension	Value
Rotor	Height (mm)	26.0
	Outer diameter (mm)	24.0
	Inner diameter (mm)	10.0
	Shaft diameter (mm)	3.0
Stator	Height (mm)	26.0
	Outer diameter (mm)	47.0
	Inner diameter (mm)	27.0
	Mount hole length (mm)	5.0
	Mount hole width (mm)	1.5
	Mount hole depth (mm)	5.0
Commutator	Height (mm)	10.0
	Outer diameter (mm)	8.0
	Shaft diameter (mm)	3.0

The coupling mechanism was also designed and modelled using Autodesk Fusion, based off of the ACOR connector. The design decoupled the connector from the transmitting and receiving of data and used it purely as a structural way to link modular units together. The design also scaled down the connector and reduced the number of latches to four. These changes simplified the connector design making it easier to model. The latch also featured through-holes to integrate the SMA wire as the primary way of actuation. The design friction fitted the latches into the front cover of the motor in a circular pattern. The front cover also included a through-hole for a bearing to be friction fitted to allow the shaft to spin freely while the motor was in operation. With the latch acting as the male component, the female component was designed as a circular ring recessed from the internal wall, which was incorporated in the back cover of the motor. All dimensions and models relating to the Latch, Front Cover, and Back Cover are shown in Table 2 and Fig. 10.

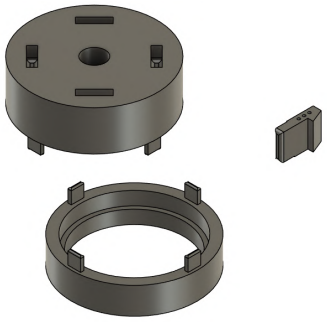

Fig. 10. 3D Models of Latch, Front and Back Motor Covers

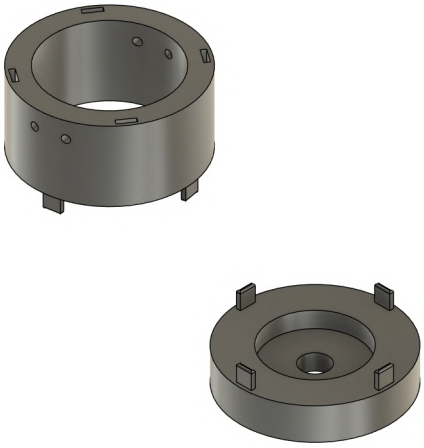

Fig. 11. 3D Models of Ring 1 and Ring 2

Table 2. Dimensions of Latch, Front and Back Covers

	Dimension	Value
Latch	Height (mm)	15.0
	Thickness (mm)	3.0
	SMA hole diameter (mm)	1.0
	Latching distance (mm)	2.0
	Fillet (mm)	1.0
Front Cover	Height (mm)	15.0
	Outer diameter (mm)	47.0
	Bearing diameter (mm)	8.0
	Latch hole length (mm)	10.0
	Latch hole width (mm)	3.0
	Latch hole depth (mm)	5.0
	Mount protrusion length (mm)	4.75
	Mount protrusion width (mm)	1.25
	Mount protrusion height (mm)	5.0
Back Cover	Height (mm)	10.0
	Outer diameter (mm)	47.0
	Inner diameter (mm)	37.0
	Ring recessed distance	2.0
	Mount protrusion length (mm)	4.75
	Mount protrusion width (mm)	1.25
	Mount protrusion height (mm)	5.0

The last components of the modular unit is two spacer rings that go between the stator and the front and back covers. Ring 1 acts as a mounting spot for 1mm copper wire to be able to connect them to the commutator, effectively using them as brushes to power the motor. Ring 2 features a through-hole for a bearing which works in tandem with the bearing in the front cover to ensure the motor shaft is centered inside the stator. All dimensions and models for Ring 1 and Ring 2 can be seen in Table 3 and Fig. 11.

Table 3. Dimensions of Ring 1 and Ring 2

	Dimension	Value
Ring 1	Height (mm)	22.0
	Outer diameter (mm)	47.0
	Inner diameter (mm)	35.0
	Copper wire hole diameter (mm)	1.5
	Mount hole length (mm)	5.0
	Mount hole width (mm)	1.5
	Mount hole depth (mm)	5.0
Ring 2	Height (mm)	10.0
	Outer diameter (mm)	47.0
	Inner diameter (mm)	27.0
	Bearing diameter (mm)	8.0
	Mount protrusion length (mm)	4.75
	Mount protrusion width (mm)	1.25
	Mount protrusion height (mm)	5.0

3.2 Material selection and printing

Different parts of the MRR unit required different materials based on their function. The materials chosen for 3D printing were Polylactic Acid (PLA) filament, Thermoplastic polyurethane (TPU) and Protopasta Iron-filled PLA. PLA was chosen as it is easily accessible and a standard printing material that could be used for structural component. TPU was used as it is a flexible material that maintains its strength and can flex without breaking if acted on by the SMA actuator. This makes it an excellent material for the latches of the modular unit. The Protopasta filament was chosen as the material for the rotor and stator as it has required magnetic properties.

A Bambu Labs P1S printer was used to manufacture the parts of the modular unit. Table 4 shows the printer settings that were used for each material. The PLA and TPU

used a 0.4mm hardened steel nozzle while the Protopasta magnetic iron-filled filament required a 0.6mm hardened steel nozzle for the printing process as it contains Iron particles that would damage or clog the 0.4mm nozzle.

Table 4. P1S Printer Settings for Different Materials

Material	Parameter	Value
PLA	Nozzle Temperature (°C)	220
	Bed Temperature (°C)	60
	Volumetric Speed (mm^3/s)	12
TPU	Nozzle Temperature (°C)	215
	Bed Temperature (°C)	45
	Volumetric Speed (mm^3/s)	5
Iron-filled	Nozzle Temperature (°C)	192
	Bed Temperature (°C)	60
	Volumetric Speed (mm^3/s)	2.5

The components of the modular unit that required similar materials and printer settings were grouped together to allow for a more efficient printing process. Table 5 shows how the different components were grouped together and what materials they required. The magnets used in the motor were also printed using a spherical powder called MQP-S-11-9 from Neo Magnequench. The chemical composition of this powder can be seen in Table 6.

Table 5. Printing Groups for Modular Unit Components

	Grouping	Printer Process Setting	Material
1	Rotor Stator	0.3mm Standard	Iron-filled
2	Commutator	0.08mm High Quality	PLA
3	Front Cover Back Cover Ring 1 Ring 2	0.2mm Standard	PLA
4	Latches	0.08mm High Quality	TPU

Table 6. Chemical Composition of MQP-S-11-9

Chemical	Percentage (%)
Neodymium	17.2
Praseodymium	1.9
Boron	1.7
Cobalt	2.8
Copper	0.1
Titanium	2.1
Zirconium	4.3
Carbon	0.1
Iron	69.8

A Computer-Aided Design (CAD) model was developed using Autodesk Fusion for the cylindrical magnets which were 6mm in diameter and 10mm tall. 20 cylinders were imported into Quant AM, a slicing software used to place the cylinders on the build plate. The software sliced out the cylinders into a total of 167 layers. The MQP-S -11- 9 powder was loaded into the machine, and everything was prepared for the print. The print took a total of 2.5 hours and can be seen in Fig.12. The parts were cut off from the plate by manual sawing. The samples will be coated with an epoxy resin before magnetizing to prevent them from falling apart. The 3D printing of rare earth magnets is quite challenging as cracking, delamination and porosity are usually observed in this type of material. The magnets that were printed had a low porosity and no delamination was observed, however they were prone to cracking which could affect their magnetic properties, however this has yet to be studied.

Fig. 12. 3D printed rare earth magnets

3.3 Assembly

Once all the parts of the modular unit were printed, they could then be assembled and tested. The iron core that was printed for the rotor was fitted with a metal shaft and had copper wire wound between the slots. A PLA commutator was also attached with copper ribbons and fitted onto the shaft so that the ends of the copper windings could be soldered to it. This formed the rotor shown in Fig. 13.

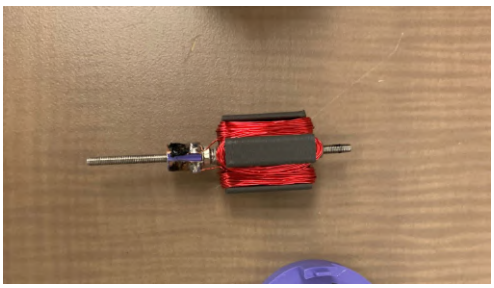

Fig. 13. 3D printed Rotor with Copper Windings

The 3D printed magnets have not been magnetized as yet and so for experimental purposes, Neodymium magnets were placed in the stator in the slots that were designed for the 3D printed magnets. The stator was then fitted onto a spacing ring that was printed and then attached to the back cover which would attach to the SMA actuated coupling mechanism. The rotor was then placed into the stator and bearings were used to keep the shaft in place while still allowing rotation of the rotor. This can be seen in Fig.14.

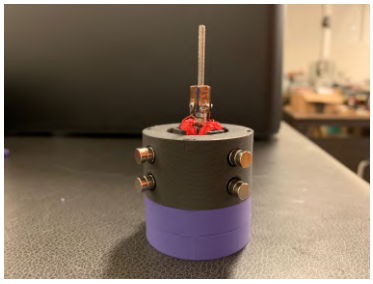

Fig. 14. Rotor and stator assembled

The second PLA ring was fitted with Copper leads that would make contact with the commutator to allow for the brushed DC motor operation. This ring was then placed on top of the stator and positioned so that the leads would meet the commutator surface. A top cover was then fitted with a bearing to hold the top section of the rotor shaft (see Fig.15).

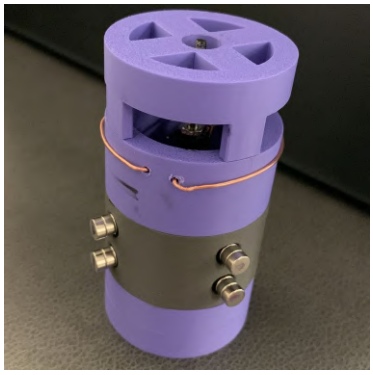

Fig. 15. Assembled 3D printed motor section of the Modular Unit

The coupling mechanism was assembled by fitting the TPU latches into the slots in a PLA printed base. SMA wire was then run through the latches and copper wire was used to form leads that could be powered as seen in Fig.16. This section could then connect to the bottom section of the motor unit and latch together.

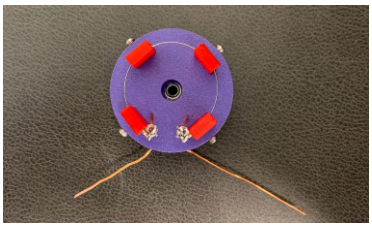

Fig. 16. 3D printed coupling mechanism

4. Theory and calculation

As one of the requirements was to focus on manual control with later iterations focusing on data storage and processing. The main control mechanisms used to operate the electrical circuits are switches and potentiometers.

4.1 H-bridge circuit

Based on experiments, the 3d-printed DC motor was most optimally operated at 10V exhibiting a peak current of 4A. Therefore, the chosen P-channel and N-channel MOSFETs to build the H-bridge circuit were the IRF9540 and IRF540 respectively. A supply voltage of 12V was used to properly account for the voltage drop across the MOSFETs. Each MOSFET in the H-bridge would be individually operated by a switch. Additionally, 10kΩ pull-up resistors and pull-down resistors were used on the gates of the IRF9540 and IRF540 respectively, to ensure that all the MOSFETs were in the off state when the switches were opened. The 1N4001 diode was chosen to act as flyback diodes in the H-bridge circuit. The main electrical characteristics of the chosen MOSFETs and diode can be seen in Table 7. The electrical circuit diagram and constructed circuit for the H-bridge are shown in Fig. 17 and Fig. 18 respectively.

Table 7. Electrical Characteristics of IRF9540, IRF540, 1N4001 [28–30]

	Characteristic	Value
IRF9540	Drain-source voltage limit (V)	-100.0
	Gate-source voltage limit (V)	±20.0
	Continuous drain current limit (A)	-19.0
	Gate-source rec. voltage (V)	-10.0
	Drain-source on resistance (Ω)	0.2
IRF540	Drain-source voltage limit (V)	100.0
	Gate-source voltage limit (V)	±20.0
	Continuous drain current limit (A)	28.0
	Gate-source rec. voltage (V)	10.0
	Drain-source on resistance (Ω)	0.077
1N4001	Max reverse voltage (V)	50.0
	Max forward current (A)	1.0

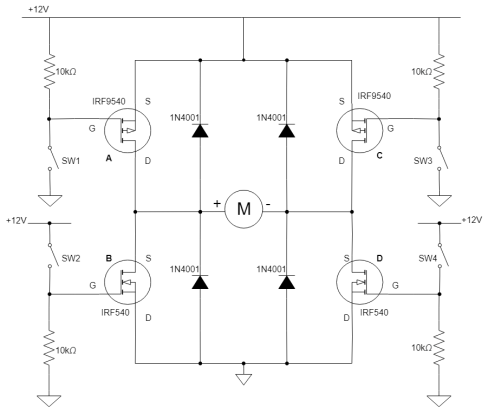

Fig. 17. Electrical circuit diagram of H-bridge

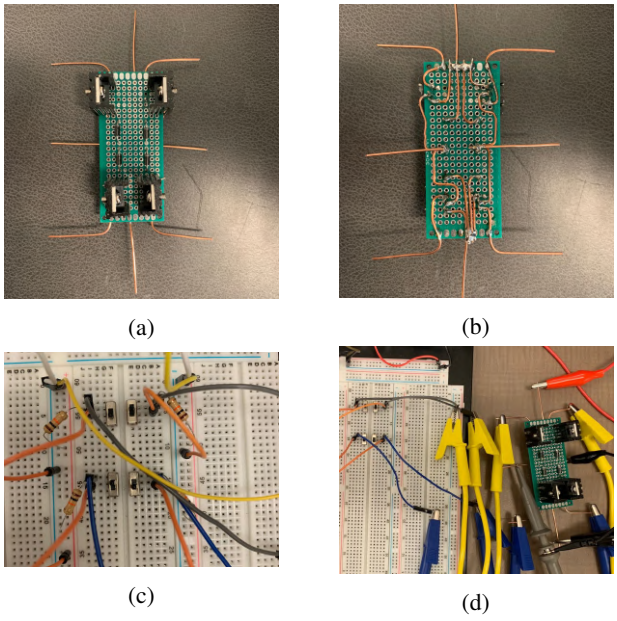

(a) (b) (c) (d)

Fig. 18. Constructed circuit of H-bridge showing: (a) Front view, (b) Back view, (c) Switches with pull-up and pull-down resistors, and (d) Complete setup

A major consideration for the H-bridge circuit is the possibility of shoot-through (short-circuiting the supplying to ground) due to improper configurations of the switches (SW1 - SW4). To prevent this scenario, a truth table of all possible switch combinations are shown in Table 8.

Table 8. Truth Table of Possible Switch Combinations

SW1	SW2	SW3	SW4	Result
open	open	open	open	OC**
open	open	open	close	OC**
open	open	close	open	OC**
open	open	close	close	SC*
open	close	open	open	OC**
open	close	open	close	0V
open	**close**	**close**	**open**	**-12V**
open	close	close	close	SC*
close	open	open	open	OC**
close	**open**	**open**	**close**	**+12V**
close	open	close	open	0V
close	open	close	close	SC*
close	close	open	open	SC*
close	close	open	close	SC*
close	close	close	open	SC*
close	close	close	close	SC*

* SC = Short-circuit
** OC = Open-circuit

From Table 8, it can seen that there are only two valid configurations for the switches that yield the desired results. Configuration 1 can be considered forward polarity for the DC motor which will see +12V across its inputs, while configuration 2 would be reverse polarity and the DC motor will see -12V across its inputs. Configuration 1 can be achieved by closing SW1 and SW4 while leaving the other switches open. Configuration 2 is the inverse of configuration 1 where SW2 and SW3 are closed but SW1 and SW4 remains opened.

4.2 PWM generator circuit

Using the circuit from [25] as a baseline, the triangular waveform generator utilized LM741 operational amplifiers because their slew rate was suitable for our chosen PWM frequency of 1kHz [31]. The circuit was adapted to use two comparators, where the inputs of one comparator would be flipped to produce a complimentary PWM signal. This is required for the gate drive of the N-channel and P-channel MOSFETs in the H-bridge. IT should be noted that the triangular waveform would act as the reference voltage for the comparator and the other input voltage would be controlled by a potentiometer that would vary the voltage and hence vary the PWM duty cycle. The LM358 was the chosen operational amplifier for the comparator due to its short-circuited protected outputs [32]. The LM741 and LM358 are both widely available and inexpensive which would make them ideal for the initial prototype. The discrete electrical components to complete the PWM generator circuit are shown in Table 9.

Table 9. Electrical Components of PWM Generator

	Symbol (Unit)	Value
Resistors	R_1 (kΩ)	4.7
	R_2 (kΩ)	1.0
	R_3 (kΩ)	2.0
	R_{pot} (kΩ)	10.0
Capacitors	C_1 (μF)	0.1
	C_2 (μF)	3.3

The resulting PWM frequency based on Table 9, is calculated using Equation 1 given by [25].

$$\begin{aligned} f &= \frac{R_3}{4R_1R_2C_1} \\ &= \frac{2 \times 10^3}{4(4.7 \times 10^3)(1 \times 10^3)(0.1 \times 10^{-6})} \\ &= 1.06kHz \end{aligned} \quad [1]$$

The calculated frequency from Equation 1 is approximately equal to our chosen frequency of 1kHz, which means the circuit will meet our design requirements. The complete electrical circuit diagram and associated constructed circuit are shown in Fig. 19 and Fig. 20.

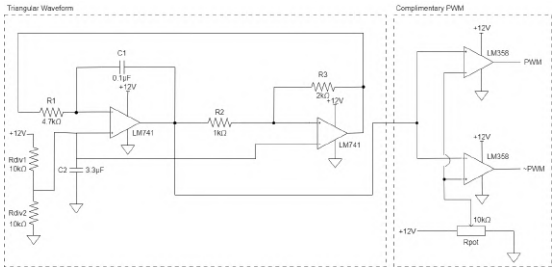

Fig. 19. Electrical Circuit Diagram of PWM Generator

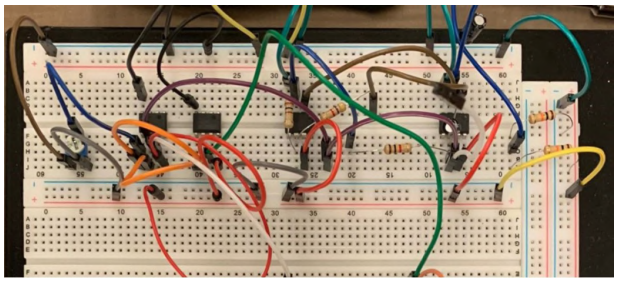

Fig. 20. Constructed Circuit of PWM Generator

5. Results and discussion

From 4.1, there are only two valid configurations of switches that will yield the desired results of forward and reverse polarity. These switch combinations are tested and verified using an oscilloscope as shown in Fig. 21b.

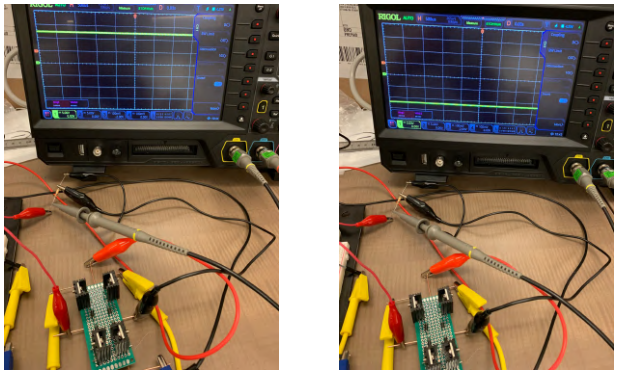

(a) (b)

Fig. 21. Oscilloscope setup with H-bridge circuit showing: (a) Configuration 1 Forward Polarity +12V, and (b) Configuration 2 Reverse Polarity -12V

From 4.2, complimentary PWM waveforms with a frequency of approximately 1kHz or period of 1ms was tested and verified using an oscilloscope as shown in Fig. 22. The adjusting of the PWM duty cycle via the potentiometer was also tested and verified in Fig. 23.

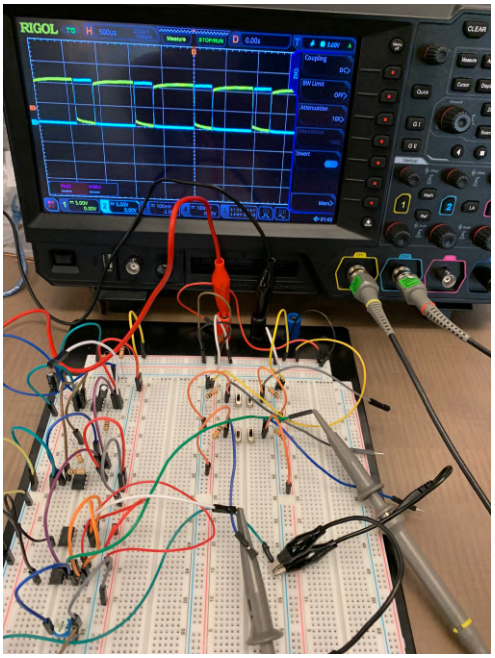

Fig. 22. Frequency test of PWM generator using oscilloscope

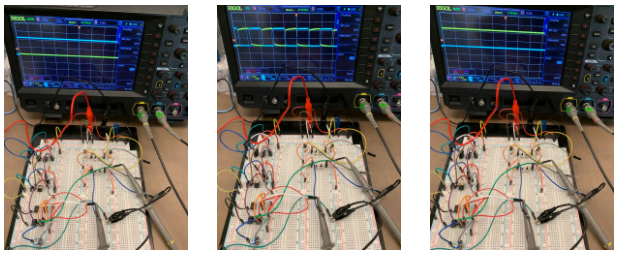

(a) (b) (c)

Fig. 23. Oscilloscope setup with PWM generator circuit showing: (a) 0% Duty cycle, (b) 50% duty cycle, and (c) 100% duty cycle

Therefore, results show that the H-bridge and PWM generator circuit is working as intended and can be integrated to create a variable speed open loop control of the DC motor in both forward and reverse directions.

From 3.3, the assembled DC motor was tested and it was verified that it generated enough torque to start spinning with a no load current of approximately 1.5A (see. Fig 24).

This high no-load current can mainly be attributed to the effect of friction on the 3D-printed DC motor. A possible solution is to use lubricants to minimize friction between the commutator and copper leads as well as between the shaft and bearings.

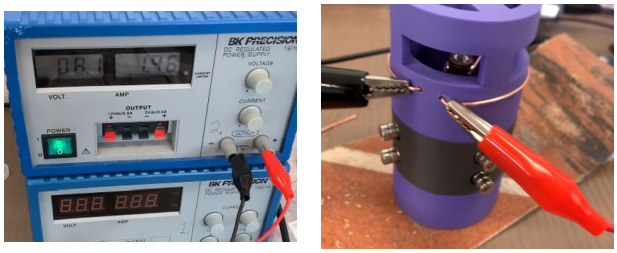

(a) (b)

Fig. 24. Pictures of DC motor spinning showing: (a) 1.5A no-load current, and (b) Commutator sparks

From 3.3, the coupling mechanism using the SMA wire was tested and it was verified that the wire exerted enough force to contract the latches but only by 1mm and not the required amount of 2mm (see Fig. 25). However, it was also verified that the latches were able to return to their original shape and did not experience plastic deformation (see Fig. 25). Possible solutions for this are to increase the number of loops of SMA wire as well as increase the height of the latches to minimize the force required.

A major noticeable limitation of the TPU latches, is that after repeated uses the SMA wire would eventually melt through the plastic. Alternatively, 3D-printing materials like carbon nylon may withstand the temperatures of the SMA wire.

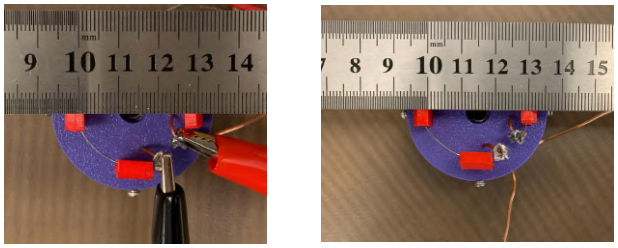

(a) (b)

Fig. 25. Coupling mechanism showing: (a) Actuation by SMA wire, and (b) Latches returning to original shape

6. Conclusions and future work

The work done demonstrated that a DC motor can be 3D-printed using special iron-filled filament. The DC-motor was small at 47mm in diameter and was able to operate with a no-load current of 1.5A. The motor was successfully integrated in the modular reconfigurable unit along with the electronic circuitry and coupling mechanism. Future work includes investigating alternative coupling mechanisms like the hook type using SMA springs, expanding the control system to include a electrical circuit P-controller with the addition of a sensor to close the control loop. Additionally, the motor would be tested again when the 3D-printed magnets are magnetized to compare the performance.

Acknowledgements

We would like to express our sincere gratitude to the National Research Council for generously providing the powder used for the 3D printing process of the rare earth magnets. Also, our sincere appreciation to GreenAge Materials and Mitacs for funding the 3D printing of rare earth magnets. We would also like to deeply thank Prof. Mihaela Vlasea for her invaluable support leading the research on 3D printing rare earth magnets. Additionally, we would like to extend our appreciation to Dr. Mohsen Keshavarz for coordinating the efforts on printing with this type of material. Finally, we would also like the thank Mr. Xavier Walls Perez for facilitating the 3D Printing correspondence with the team at the University of Waterloo and at the National Research Council.

References

[1] J. Seo, J. Paik, and M. Yim, “Modular reconfigurable robotics,” *Annual Review of Control, Robotics, and Autonomous Systems*, vol. 2, no. 1, pp. 63–88, 2019.

[2] M. Yim *et al.*, "Modular self-reconfigurable robot systems [grand challenges of robotics]," *IEEE Robotics & Automation Magazine*, vol. 14, no. 1, pp. 43–52, 2007.

[3] A. M. Romanov, V. D. Yashunskiy, and W.-Y. Chiu, "A modular reconfigurable robot for future autonomous extraterrestrial missions," *Ieee Access*, vol. 9, pp. 147 809–147 827, 2021.

[4] S.-H. Kim, *Electric motor control: DC, AC, and BLDC motors*. Elsevier, 2017.

[5] F. Giri, *AC electric motors control: advanced design techniques and applications*. John Wiley & Sons, 2013.

[6] R. Condit, "Brushed dc motor fundamentals," *Microchip Application Note AN905, Microchip Technology Inc*, 2004.

[7] P. Yedamale, "Brushless dc (bldc) motor fundamentals," *Microchip Technology Inc*, vol. 20, no. 1, pp. 3–15, 2003.

[8] R. Parekh, "Ac induction motor fundamentals," *Microchip Technology Inc*, no. DS00887A, pp. 1–24, 2003.

[9] R. Gambhir and A. K. Jha, "Brushless dc motor: Construction and applications," *Int. J. Eng. Sci*, vol. 2, no. 5, pp. 72–77, 2013.

[10] K. Kamel and K. Anissa, "Design and implementation of microcontroller based controller for direction and speed of a robot using arduino," *no. May*, vol. 2016, 2016.

[11] K. Yılmaz, "Comparison of axial flux and radial flux brushless dc motor topologies for control moment gyroscope wheel applications," M.S. thesis, Middle East Technical University, 2009.

[12] A. Y. Hassan, A. G. Rohieem, and S. M. S. Salem, "Direct torque control of non-salient pole afpmsms with svpwm inverter," *International Journal of Power Electronics and Drive Systems (IJPEDS)*, vol. 13, no. 4, pp. 2014–2023, 2022.

[13] K. Sitapati and R. Krishnan, "Performance comparisons of radial and axial field, permanent-magnet, brushless machines," *IEEE Transactions on industry applications*, vol. 37, no. 5, pp. 1219–1226, 2001.

[14] T. Genberg, "Motor fundamentals: E-learning course," 2017.

[15] A. Othman, N. Hamzah, Z. Hussain, R. Baharudin, A. D. Rosli, and A. I. C. Ani, "Design and development of an adjustable angle sensor based on rotary potentiometer for measuring finger flexion," in *2016 6th IEEE International Conference on Control System, Computing and Engineering (ICCSCE)*, IEEE, 2016, pp. 569–574.

[16] R. K. Megalingam, S. Boddupalli, and K. Apuroop, "Robotic arm control through mimicking of miniature robotic arm," in *2017 4th International Conference on Advanced Computing and Communication Systems (ICACCS)*, IEEE, 2017, pp. 1–7.

[17] S. Paul, J. Chang, J. E. Fletcher, and S. Mukhopadhyay, "A novel high-resolution optical encoder with axially stacked coded disk for modular joints: Physical modeling and experimental validation," *IEEE Sensors Journal*, vol. 18, no. 14, pp. 6001–6008, 2018.

[18] Y. Xu *et al.*, "The boom in 3d-printed sensor technology," *Sensors*, vol. 17, no. 5, p. 1166, 2017.

[19] W. Saab, P. Racioppo, and P. Ben-Tzvi, "A review of coupling mechanism designs for modular reconfigurable robots," *Robotica*, vol. 37, no. 2, pp. 378–403, 2019.

[20] M.-S. Kim *et al.*, "Shape memory alloy (sma) actuators: The role of material, form, and scaling effects," *Advanced Materials*, vol. 35, no. 33, p. 2 208 517, 2023.

[21] A. Ellery and A. Elaskri, "3d printing modules for self-assembling space systems," 2024.

[22] M. Badescu and C. Mavroidis, "Novel active connector for modular robotic systems," *IEEE/ASME transactions on mechatronics*, vol. 8, no. 3, pp. 342–351, 2003.

[23] A. Spröwitz *et al.*, "Roombots: Reconfigurable robots for adaptive furniture," *IEEE Computational Intelligence Magazine*, vol. 5, no. 3, pp. 20–32, 2010.

[24] M. B. Ranadev and R. Chakrasali, "Speed-torque characteristic of dc motor fed by h-bridge converter," *International Journal of Energy and Power*, vol. 3, no. 4, pp. 49–53, 2014.

[25] M. I. Products, "Pulse-width modulator operates at various levels of frequency and power," Maxim Integrated Products, Tech. Rep., 2004.

[26] T. K. Swain and V. Baid, "Analog fabrication of pid controller," Ph.D. dissertation, 2014.

[27] B. Lynch, X.-X. Jiang, A. Ellery, and F. Nitzsche, "Characterization, modeling, and control of ni-ti shape memory alloy based on electrical resistance feedback," *Journal of Intelligent Material Systems and Structures*, vol. 27, no. 18, pp. 2489–2507, 2016.

[28] *Power mosfet*, IRF9540, Rev. C, Vishay Siliconix, Aug. 2021.

[29] *Power mosfet*, IRF540, Rev. C, Vishay Siliconix, Aug. 2021.

[30] *General purpose plastic rectifier*, IRF540, Rev. A, Vishay General Semiconductor, Apr. 2020.

[31] *General-purpose operational amplifiers*, LM741, Rev. D, Texas Instruments, Oct. 2015.

[32] *Single supply dual operational amplifiers*, LM358, Rev. 36, ONSEMI, Sep. 2024.